



## OPEN ACCESS

## EDITED BY

Maxim Lebedev,  
Edith Cowan University, Australia

## REVIEWED BY

Danqing Song,  
South China University of Technology,  
China  
Bing Bai,  
Beijing Jiaotong University, China  
Mukhtiar Ali Soomro,  
Quaid-e-Awam University of  
Engineering, Pakistan

## \*CORRESPONDENCE

Wen-Chieh Cheng,  
✉ w-c.cheng@xauat.edu.cn

RECEIVED 14 February 2023

ACCEPTED 03 July 2023

PUBLISHED 18 July 2023

## CITATION

Wen S, Cheng W-C, Hu W and  
Rahman MM (2023), Changes in air and  
liquid permeability properties of loess due  
to the effect of lead contamination.  
*Front. Earth Sci.* 11:1165685.  
doi: 10.3389/feart.2023.1165685

## COPYRIGHT

© 2023 Wen, Cheng, Hu and Rahman.  
This is an open-access article distributed  
under the terms of the [Creative  
Commons Attribution License \(CC BY\)](#).  
The use, distribution or reproduction in  
other forums is permitted, provided the  
original author(s) and the copyright  
owner(s) are credited and that the original  
publication in this journal is cited, in  
accordance with accepted academic  
practice. No use, distribution or  
reproduction is permitted which does not  
comply with these terms.

# Changes in air and liquid permeability properties of loess due to the effect of lead contamination

Shaojie Wen<sup>1,2</sup>, Wen-Chieh Cheng<sup>1,2\*</sup>, Wenle Hu<sup>1,2</sup> and  
Md Mizanur Rahman<sup>3</sup>

<sup>1</sup>School of Civil Engineering, Xi'an University of Architecture and Technology, Xi'an, China, <sup>2</sup>Shaanxi Key Laboratory of Geotechnical and Underground Space Engineering (XAUAT), Xi'an, China, <sup>3</sup>UniSA STEM, SIRM, University of South Australia, Adelaide, SA, Australia

Heavy metals in landfill leachate are easily adsorbed by soil particles, causing serious threats to human health and surrounding environments. Mining and metallurgy activities are intensive in Northwest China, thereby enlarging threats. The aim of the present study is to enhance our knowledge about the linkage between the microstructural evolution of the loess soil induced by lead contamination and the macro air and liquid permeability properties. A series of air and liquid permeability tests on the uncontaminated and Pb-contaminated loess specimens were conducted. Their air and liquid permeability properties were evaluated on the basis of Darcy's law and the soil-water retention curves, respectively. The microstructural evolution, when subjected to low and high Pb<sup>2+</sup> concentrations, was assessed using scanning electron microscopy (SEM), X-ray diffraction (XRD), mercury intrusion porosimetry (MIP), and zeta potential tests. The intrusion of Pb<sup>2+</sup> decreases the absolute zeta potential  $\zeta$ , which in turn leads to a more distinct agglomerated structure and higher intrinsic permeability. Moreover, the dedolomitization and associated cerussite (PbCO<sub>3</sub>) precipitation are deemed as the main cause of micropore clogging, whereas the corrosion of the cement between soil particles by H<sup>+</sup> shows a good correspondence to an increase in the number of mesopores. With the concentration of Pb<sup>2+</sup> increasing from 0 to 2,000 mg/kg, the proportion of micropores decreases from 37.9% to 15.1%, and the proportion of mesopores increases from 17.3% to 53.3%. In addition, the air entry value decreased from 19.5 to 12.8 kPa, indicating that the water retention behavior decreased. The findings highlight the impacts of lead contamination on the microstructure and macro permeability properties and give some design guideposts to heavy metal-contaminated site remediation.

## KEYWORDS

loess, lead, air permeability, water retention, diffuse double layer, diffuse dedolomitization

## 1 Introduction

Rapid urbanization and population growth over the last few years have resulted in a huge generation of municipal solid waste (MSW). In China, nearly 235 million tons of MSW were collected in the cities accommodating 902 million urban residents in 2020 (NBSPRC, 2021). MSW landfills are the dominant option for waste disposal in many developed/developing countries due to their simple operation, low cost, and large disposal capacity (Laner et al.,

2012; Zhan et al., 2017a). For example, in China, there are 644 active landfills for the disposal of the MSW generated, and approximately 33% of the 235 million tons of MSW generated was landfilled in 2020 (NBSPRC, 2021). There are numerous hazardous compounds in landfill leachate due to the unscientific collection, classification, and disposal methods of MSW (Bai et al., 2021; Wen et al., 2023a; Gao et al., 2015; Naveen et al., 2017; Negi et al., 2020). Due to biodegradation, the landfill air of MSW increases the pressure within landfills (Xu Y. et al., 2021; Shi et al., 2021; Xie et al., 2023; Xue et al., 2021) and thereby promotes the escape of leachate and landfill air from the landfill (Moon et al., 2007; Bian et al., 2021; Hu et al., 2022). The leachate, in particular, is a major geoenvironmental concern as heavy metals in leachate are adsorbed onto soil particles by cation exchange or chemisorption and clump formation due to their capacity to form strong metallic bonds (Wang et al., 2009; Burakov et al., 2017; Naveen et al., 2017), which will increase the permeability of compacted soil (Souli et al., 2008; Zha et al., 2021). Therefore, there is a pressing need to investigate the engineering properties of heavy metal-contaminated soils, particularly their permeability.

In recent years, research on the engineering properties of heavy metal-contaminated soils has attracted extensive attention. Dutta and Mishra (2016) found that the permeability of contaminated soils increases with an increase in the heavy metal concentration. Souli et al. (2008) observed that soil permeability increased with an increase in  $Zn^{2+}$  concentration. Li et al. (2015), Dutta and Mishra (2016), and Zha et al. (2021) indicated that the changes in geotechnical properties and microstructure caused by heavy metals could be interpreted by diffuse double layer (DDL) theory. Contaminant transport and leaching processes are strictly unsaturated fluid transport phenomena (Lu & Likos, 2004). Generally speaking, the movement of pore water and pore air in unsaturated soil is the focus of the research on the permeability of unsaturated soils. Various studies have been conducted over recent years to link air permeability with dry density, liquid saturation, and pore size (Zhan et al., 2014; Chen et al., 2017; Xu L. et al., 2020). Some studies on liquid permeability have concentrated on the influences of liquid saturation and dry density (Wang H. K. et al., 2020; Pandey et al., 2021). However, previous studies on the permeability of unsaturated soils were performed at air permeability or liquid permeability, and very little data regarding the functional relationship between liquid permeability and air permeability have been reported, except for the tests reported by Zhang D. F. et al. (2020) and Zhan et al. (2017a). However, they did not consider the effect of heavy metals on the liquid permeability and air permeability of unsaturated soils. Thus, the loess has a large adsorption capacity for heavy metals (Tang et al., 2008; Wang et al., 2016). In other words, once the leachate leaks, the heavy metals in the leachate will be adsorbed by loess. In addition, the loess has been used as an earthen final cover (EFC) material on a small scale (Zhan et al., 2014). The Chinese Loess Plateau (CLP) is located in the central and western parts of China and formed in arid and semi-arid climatic conditions, and the widely distributed loess is a typical unsaturated soil (Wen et al., 2023b; Bai et al., 2022; Hu et al., 2023; Zhang D. F. et al., 2020). The loess has great potential as an EFC material (Xue et al., 2023; Wang et al., 2023; Zhan et al., 2016; Zhan et al., 2017b). Therefore, it is urgent to study the liquid and air permeability of unsaturated heavy metal-contaminated loess.

The permeability of soils is mainly controlled by their microstructure, such as the pore size distribution, void ratio, and connectivity among pores (Cai et al., 2014; Elhakim, 2016; Liu and Jeng, 2019; Wang J. D. et al., 2020; Wei et al., 2020; Xu P. P. et al., 2021). Some research efforts have investigated the relationships between the microstructure and permeability of soil (Chen et al., 2019; Xu J. et al., 2020; Zhang J. et al., 2020). Hong et al. (2019) found that the pore structure of Malan loess showed good connectivity in the horizontal direction, and the horizontal direction was more permeable than the vertical direction. Zhou et al. (2021) illustrated that a decrease in the volume and diameter of pores could reduce permeability. The same conclusions were made by Gao et al. (2018) when an attempt was made to link permeability and the microstructure of lime-treated loess. Zhao et al. (2016) studied the microstructure characteristics of leachate-polluted compacted clays and found that the aggregate structure was destroyed by leachate pollution. The loess has a metastable microstructure with weak cementation and high porosity. Heavy metals are adsorbed by loess particles through cation exchange or chemisorption to form agglomerated structures, which makes the microstructure change complex. In addition, no comprehensive studies have not been conducted yet concerning the water retention and permeability of heavy metal-contaminated loess. The aforementioned study reveals a series of gaps and shortcomings that remain to be addressed. The main objectives of this study are as follows: 1) to derive the water retention curve of the uncontaminated and Pb-contaminated loess specimens for assessing its air and liquid permeability properties, 2) to assess the microscale structural evolution using scanning electron microscopy (SEM), X-ray diffraction (XRD), mercury intrusion porosimetry (MIP), and zeta potential tests considering low and high  $Pb^{2+}$  concentrations, and 3) to present a correspondence between the microscale structural evolution and the air and liquid permeability properties.

## 2 Materials and methods

### 2.1 Materials

Loess, as a contaminant transport and diffusion medium, is spread over Northwest China and is rich in carbonates and a variety of minerals. In light of the aforementioned details, the loess is widely applied as an adsorbent of contaminants and, therefore, distinguished from others. A series of block samples applied to the present work were collected at 3 m deep ground from Lantian County, Shaanxi Province. The block samples were immediately wrapped and transported back to Shaanxi Key Laboratory of Geotechnical and Underground Space Engineering (XAUAT), preventing disturbances and changes in water content. The particle size distribution curve of the loess was measured according to ASTM D7928-21e1 and D6913-04e1 (ASTM, 2010; ASTM, 2021). The liquid limit ( $\omega_L$ ) and plasticity index (PI) of the loess are 31.6% and 12.1%, respectively. The loess is classified as low-plasticity clay (CL) in accordance with the Unified Soil Classification System (USCS). The physicochemical properties of the loess are tabulated in [Supplementary Table S1](#).

TABLE 1 Summary of the testing schemes applied to the present work.

Testing scheme applied to liquid permeability tests (LT)						
Test no.	Pb <sup>2+</sup> concentration (mg/kg)	Dry density $\rho_d$ (kN/m <sup>3</sup> )	Net stress (kPa)	Air pressure (kPa)	Water pressure (kPa)	Matric suction (kPa)
LT1	0	13.7	50	30/35/50/90/150/230/330	30	0/5/20/60/120/200/300
LT2	500	13.7	50	30/35/50/90/150/230/330	30	0/5/20/60/120/200/300
LT3	1,000	13.7	50	30/35/50/90/150/230/330	30	0/5/20/60/120/200/300
LT4	2,000	13.7	50	30/35/50/90/150/230/330	30	0/5/20/60/120/200/300
Testing scheme applied to air permeability tests (AT)						
Test no.	Pb <sup>2+</sup> concentration (mg/kg)	Dry density $\rho_d$ (kN/m <sup>3</sup> )	Cell pressure (kPa)	Water content (%)	Air pressure (kPa)	
AT1	0	13.7	50	2/6/12/14/18/20/22/25	10/20/30/40	
AT2	500	13.7	50	2/6/12/14/18/20/22/25	10/20/30/40	
AT3	1,000	13.7	50	2/6/12/14/18/20/22/25	10/20/30/40	
AT4	2,000	13.7	50	2/6/12/14/18/20/22/25	10/20/30/40	

There are numerous hazardous compounds in landfill leachate (Gao et al., 2015; Naveen et al., 2017; Negi et al., 2020; Xu Y. et al., 2021; Shi et al., 2021). Lead is deemed to be a typical toxic heavy metal in landfill leachate and is featured with high bioavailability. Because lead contamination can cause significant threats to surrounding environments and human health (Taylor et al., 2010; Pareja et al., 2014), lead nitrate (Pb(NO<sub>3</sub>)<sub>2</sub>) is selected as the main contaminant applied to the preparation of Pb-contaminated specimens.

### 2.2 Specimen preparation

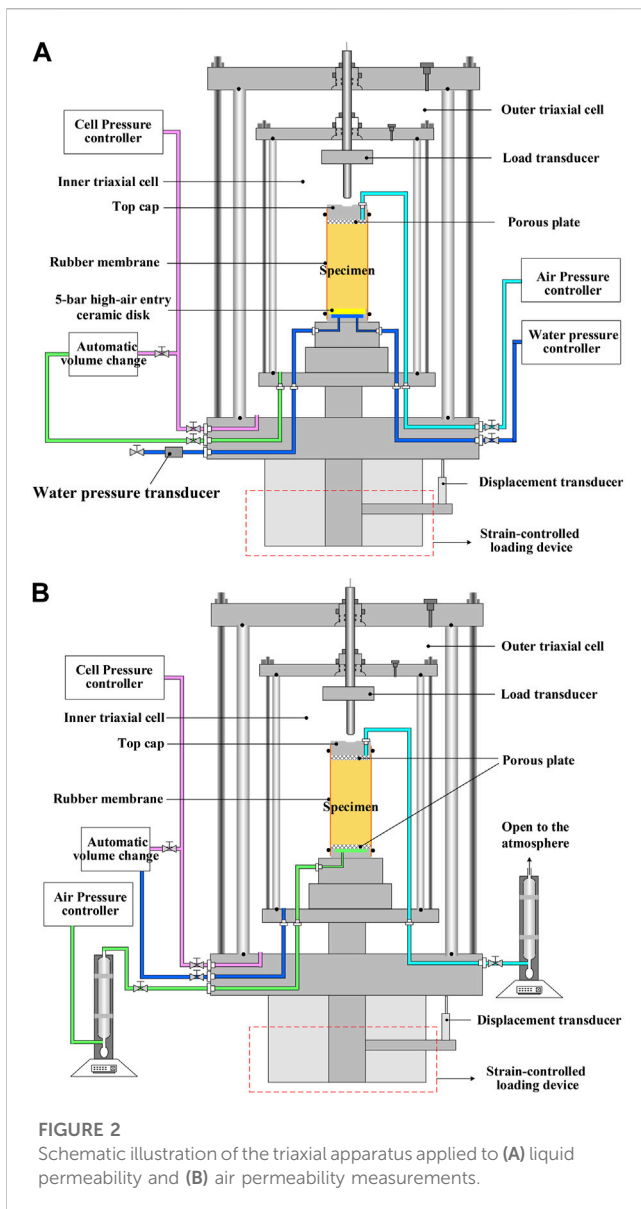
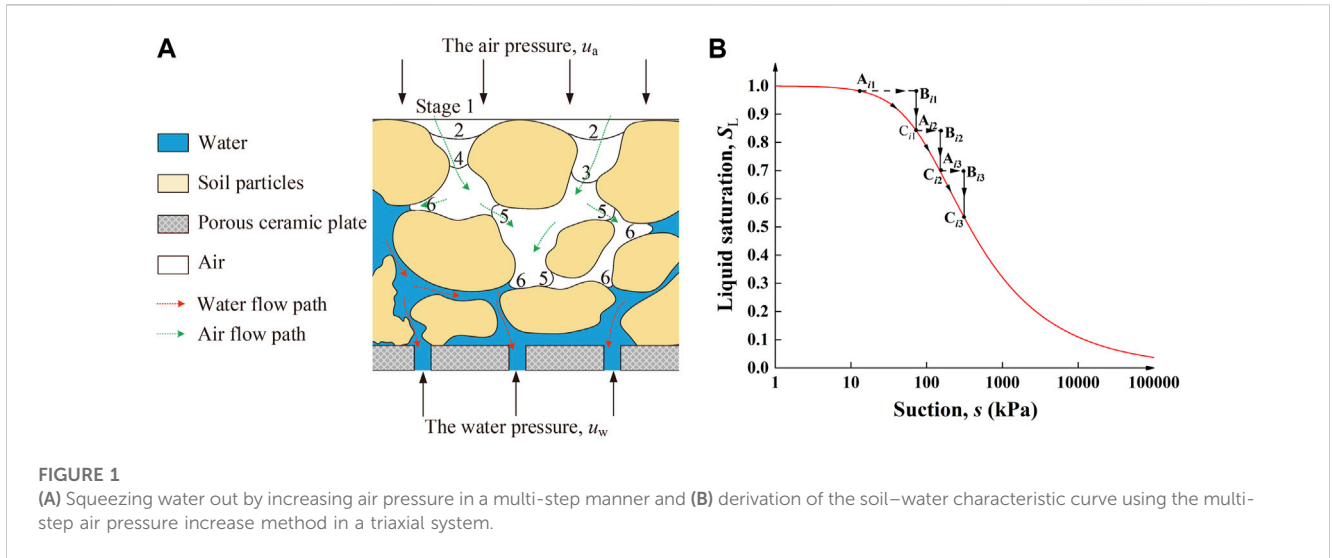
The loess was crushed, and their majority was retained using a sieve with a 2 mm mesh opening. Then, it was dried in an oven at 105°C for 24 h. The loess, Pb(NO<sub>3</sub>)<sub>2</sub>, and deionized water were weighed to prepare a Pb(NO<sub>3</sub>)<sub>2</sub> solution in the first place. Given Pb<sup>2+</sup> concentrations equal to 0, 500, 1,000, and 2,000 mg/kg, a thorough mix of loess and Pb(NO<sub>3</sub>)<sub>2</sub> solution was conducted (Du et al., 2016; Zha et al., 2021). The Pb-contaminated loess was sealed and stewed for 24 h. The Pb-contaminated loess, while preparing a cylinder specimen with a diameter of 39.1 mm and a height of 40 mm, was divided into three equal parts. Each part was loaded into a mold using the static compaction approach and with scarification between layers. A Pb-contaminated specimen with a unit weight of 15.9 kN/m<sup>3</sup> was obtained when three batches were sequentially compacted in the mold. Compared with conventional cylinder specimens of 39.1 mm diameter and 80 mm height, the height of the Pb-contaminated specimens was reduced to 40 mm to shorten the time required for achieving a matric suction equilibrium (Zhang D. F. et al., 2020; Wang J. D. et al., 2020). The Pb-contaminated specimens were then sealed in a constant temperature chamber for 10 days, thereby securing Pb<sup>2+</sup> adsorption equilibrium (Du et al., 2016; Zha et al., 2021).

### 2.3 Methods

Given that the air and liquid permeability of the Pb-contaminated loess are crucial in determining the migration of Pb<sup>2+</sup> provided landfill leachate contains lead-based contaminants, tests were designed in the present work. They are detailed in Table 1. Prior to the permeability tests, the statically compacted specimens were saturated by the vacuum saturation method, and then the drying path was applied to prevent the soil hysteresis effect.

#### 2.3.1 Liquid permeability test

In the present work, the permeability of saturated liquid was measured by the GDS permeameter, whereas the leachate was derived at the end of the permeability test for cation concentration testing. The soil suction was elevated through a drying pathway using the multi-step air pressure increase method, referred to as the “axial translation” technique (Figure 1A), to derive the soil–water characteristic curve. Given that the air pressure  $u_a$  is increased in a multi-step manner, the pore water pressure  $u_w$  is supposed to be positive, and the confining pressure  $\sigma_3$  is increased accordingly to keep the net stress ( $\sigma_3 - u_a$ ) constant in a triaxial system. An automatic unsaturated triaxial testing system (VJT9020; VJTech Limited, United Kingdom) was applied to the derivation of the soil–water characteristic curve where a



Bishop–Wesley double wall triaxial cell of 100 mm in diameter allows the inner and outer cell pressures to be kept at the same value by the cell pressure controller to eliminate the volume change due to cell expansion (Figure 2A). By adding the prescribed air pressure from the top cap, each specimen was “dried,” where the air pressure increment for a given step was applied instantaneously (i.e., from  $A_{i1}$  to  $B_{i1}$  in Figure 1B) to drive the pore water out through the high-air entry ceramic disk at the bottom cap (Figure 2A). Provided the air pressure increment starts transferring to the soil suction increment, the degree of saturation changes accordingly (i.e.,  $B_{i1}$  to  $C_{i1}$  in Figure 1B), and the water content is measured upon completion of the transfer (i.e., from  $A_{i1}$  to  $C_{i1}$  in Figure 1B). The cumulative outflow  $\Delta Q_L$  measured by the water pressure-volume controller at the end of each step was used to back-calculate the water content. As long as the equilibrium of the transfer is attained,  $u_a$  increases further to the pressure prescribed in the subsequent step. While elevating the soil suction, the aforementioned equilibrium is repeated until the final transfer reaches an equilibrium state. The advantages of the use of the multi-step air pressure increase method include 1) easing time-consuming concerns raised while applying multiple specimens to derive a soil–water characteristic curve, 2) preventing the impact of changes in pore structure using one single specimen, and 3) enhancing the accuracy of the curve-fitting parameters derived. The raw soil–water characteristic curve was curve-fitted to extract the behavior at high suction ranges using the van Genuchten (1980) equation that corresponds to one of the most common functions applied to describe the soil water retention curve (termed VG model hereafter):

$$S_{eL} = \frac{S_L - S_{RL}}{1 - S_{RL}} = \left[ \frac{1}{1 + |\alpha s|^n} \right]^m \quad (1)$$

where  $S_{eL}$  is effective liquid saturation;  $S_L$  is liquid saturation;  $S_{RL}$  is residual liquid saturation;  $\alpha$ ,  $n$ , and  $m$  ( $m = 1 - 1/n$ ) are fitting parameters; and  $s$  is matric suction (kPa). The unsaturated liquid permeability was predicted by Fredlund’s permeability model (Fredlund et al., 1994):

$$k_w(\theta_w)_i = \frac{k_s}{k_{sc}} A_d \sum_{j=i}^m [(2j+1-2i)(u_a - u_w)_j^{-2}] \quad i = 1, 2, \dots, m \quad (2)$$

$$A_d = \frac{T_s^2 \rho_L g \theta_s^p}{2\mu_L N^2} \quad (3)$$

$$N = m[\theta_s / (\theta_s - \theta_L)] \quad (4)$$

$$k_{sc} = A_d \sum_{j=i}^m [(2j+1-2i)(u_a - u_w)_j^{-2}] \quad i = 0, 1, \dots, m \quad (5)$$

where  $k_L(\theta_w)_i$  represents the liquid permeability coefficient determined by the volumetric liquid content  $(\theta_L)_i$  of the  $i$ th interval ( $\text{m}\cdot\text{s}^{-1}$ );  $i$  represents the number of intervals;  $m$  represents the interval number between saturated volume liquid content and minimum volume liquid content on the soil–water characteristic curve, taken as 20;  $k_s$  and  $k_{sc}$  are measured and calculated saturated coefficients of liquid permeability ( $\text{m}\cdot\text{s}^{-1}$ ), respectively;  $(u_a - u_w)_j$  represents suction corresponding to the  $j$ th interval (kPa);  $A_d$  represents adjusting constant ( $\text{m}\cdot\text{s}^{-1}\cdot\text{kPa}$ );  $T_s$  is surface tension of liquid, taken as  $7.28 \times 10^{-5}$  kN/m;  $\rho_L$  represents density of liquid ( $\text{kg}\cdot\text{m}^{-3}$ ) at a standard temperature of 293.15K;  $g$  is acceleration of gravity ( $\text{m}\cdot\text{s}^{-2}$ );  $\mu_L$  is liquid viscosity ( $\text{N}\cdot\text{s}\cdot\text{m}^{-2}$ );  $\theta_s$  represents saturated volumetric liquid content;  $p$  represents the constant of the interaction between pores of different sizes, taken as 2.0;  $N$  is the interval number between the saturated volume liquid content and minimum volume liquid content; and  $\theta_L$  is the minimum volume of liquid content on the soil–water characteristic curve. Liquid permeability  $K_L$  is expressed as

$$K_L = \frac{k_L \mu_L}{\rho_L g} \quad (6)$$

Furthermore, the unsaturated triaxial apparatus contains an internal pressure chamber and an external pressure chamber, and the sample overall volume change  $\Delta V$  was also measured. The void ratio  $e$  of the specimen consolidated under net stress  $(\sigma_3 - u_a)$  is calculated with the following formula:

$$e = e_n - (1 + e_n) \frac{\Delta V}{V_0} \quad (7)$$

where  $e_n$  and  $V_0$  represent the initial void ratio and initial volume of the specimen, respectively.

### 2.3.2 Air permeability test

In this study, a modification was applied to VJT9020. The bottom cap was linked to an electronic soap-film flowmeter and air supply system, whereas the top cap was connected to the other electronic soap-film flowmeter whose outlet was connected to the atmosphere (Figure 2B). The specimens contaminated at various  $\text{Pb}^{2+}$  concentrations were vacuum-saturated and then air-dried to attain eight different water contents, respectively (i.e., 2.0%, 6.0%, 12.0%, 14%, 18%, 20%, 22%, and 25%), and then sealed for at least 72 h, allowing the water content to be thoroughly equalized. The confining pressure  $\sigma_3 = 50$  kPa was applied, and air pressures  $u_a$  lower than  $\sigma_3$ , including 10, 20, 30, and 40 kPa, were applied to the bottom of the specimen using the air supply system to develop an air pressure gradient  $\Delta u_a$ . Assuming the air flux through the Pb-contaminated specimen is in a proportional relation with  $\Delta u_a$ , and their relationship is in line with Darcy's law (Fredlund &

Rahardjo, 1993; Lu & Likos, 2004), the ratio of the inflow rate  $Q_{\text{Ain}}$  to the outflow rate  $Q_{\text{Aout}}$  is, therefore, considered a key indicator that determines whether the equilibrium state of air inflow and outflow is attained. Here,  $Q_{\text{Ain}}$  and  $Q_{\text{Aout}}$  were measured by the electronic soap-film flowmeter at the bottom and top, respectively. Given the water content = 18% and degree of saturation = 57%, the equilibrium of air inflow and outflow takes approximately 2 h. In the present work, the time necessary for attaining the equilibrium state varies from 1.5 h for lower water contents to 9 h for higher water contents. Thus, the coefficient of air permeability  $k_A$  ( $\text{m}\cdot\text{s}^{-1}$ ) can be calculated by substituting the air velocity  $v_A$  ( $\text{m}\cdot\text{s}^{-1}$ ) and the air pressure gradient  $i_A$  into the following equation:

$$k_A = \frac{v_A}{i_A} = \frac{Q_A/A}{\Delta p/(\rho_A g h)} \quad (8)$$

where  $Q_A$  represents airflow rate ( $\text{m}^3\cdot\text{s}^{-1}$ );  $A$  represents cross-sectional area of the specimen ( $\text{m}^2$ );  $\Delta p$  represents air pressure difference (kPa);  $\rho_A$  is air density ( $\text{kg}\cdot\text{m}^{-3}$ ), taken as  $1.21 \text{ kg}\cdot\text{m}^{-3}$ ; and  $h$  represents specimen height (m). Air permeability  $K_A$  is expressed as

$$K_A = \frac{k_A \mu_A}{\rho_A g} = \frac{Q_A \mu_A h}{\Delta p A} \quad (9)$$

where  $\mu_A$  represents air viscosity, taken as  $1.80 \times 10^{-5} \text{ kg}\cdot\text{m}^{-1}\cdot\text{s}^{-1}$ .

### 2.3.3 SEM, XRD, MIP, and zeta potential tests

The changes in microstructural characteristics of Pb-contaminated loess were investigated by SEM. The SEM images were captured using a JEOL scanning electron microscope (JSM-7610F). The composition of major elements was analyzed by SEM images using energy-dispersive X-ray spectroscopy (SEM-EDS). Image-Pro Plus 6.0 was used to extract microstructure information, including pore size distribution and pore number. The classification for pores, as recommended by Lei (1987), refers to four categories: micropores with diameters smaller than 2  $\mu\text{m}$ , small pores with diameters between 2  $\mu\text{m}$  and 8  $\mu\text{m}$ , mesopores with diameters between 8  $\mu\text{m}$  and 32  $\mu\text{m}$ , and macropores with diameters greater than 32  $\mu\text{m}$ . The main minerals in loess were analyzed using a Bruker AXS X-ray diffractometer to investigate not only the interactions between  $\text{Pb}^{2+}$  and the loess but also its implications on the microscale structural evolution.  $\text{Pb}^{2+}$  is adsorbed to the soil particles by cation exchange or chemisorption, forming new minerals and releasing calcium ions, sodium ions, or magnesium ions into pore fluid. The changes in minerals can be detected by comparing the XRD pattern. An automatic mercury porosimeter (AutoPore Iv 9500) was applied to the MIP tests. The MIP tests are featured with a low-pressure range of 3–207 kPa and a high-pressure range of 207 kPa–413.7 MPa. They were employed to determine variations in the pore size distribution of soil samples contaminated with different concentrations of lead ions. The zeta potential of Pb-contaminated loess samples was analyzed using Malvern Zetasizer Nano ZS90 to investigate changes in the DDL of Pb-contaminated loess.

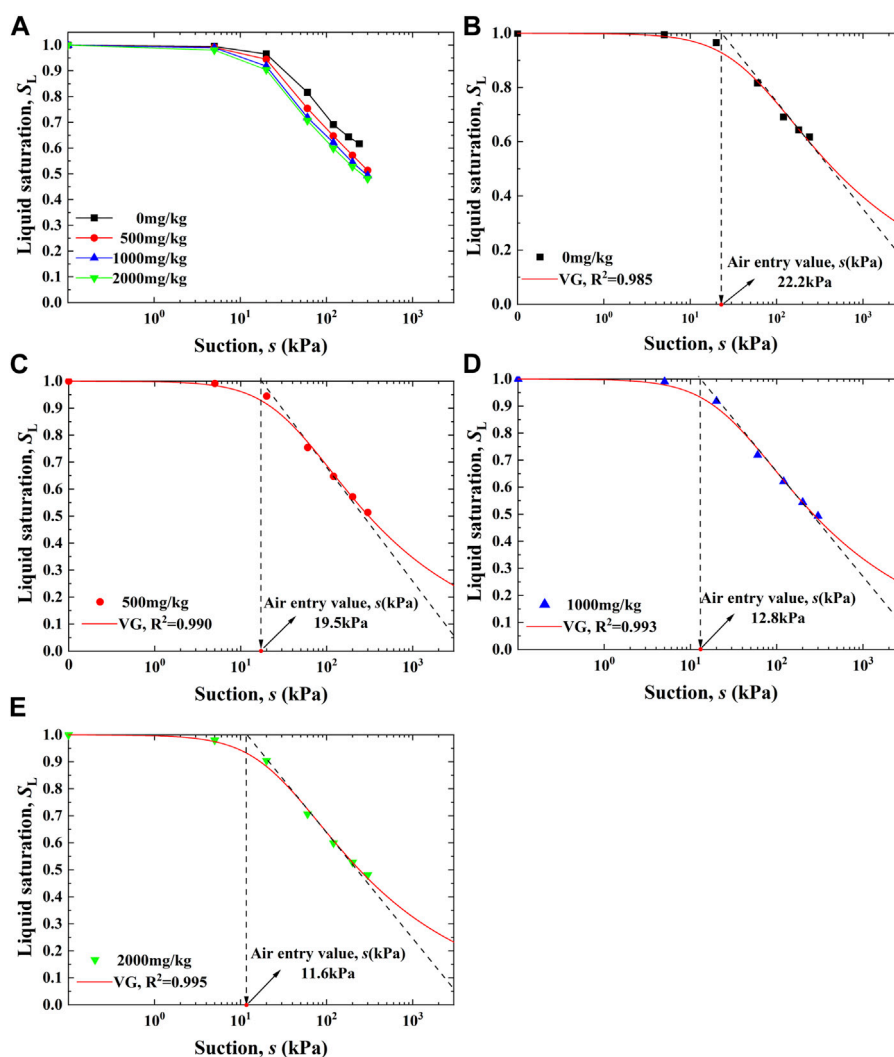


FIGURE 3

(A) Soil–water characteristic curves derived against different  $Pb^{2+}$  concentrations, (B) fitting curve using the VG model ( $Pb^{2+} = 0$  mg/kg), (C) fitting curve using the VG model ( $Pb^{2+} = 500$  mg/kg), (D) fitting curve using the VG model ( $Pb^{2+} = 1,000$  mg/kg), and (E) fitting curve using the VG model ( $Pb^{2+} = 2,000$  mg/kg).

## 3 Results

### 3.1 Water retention behavior

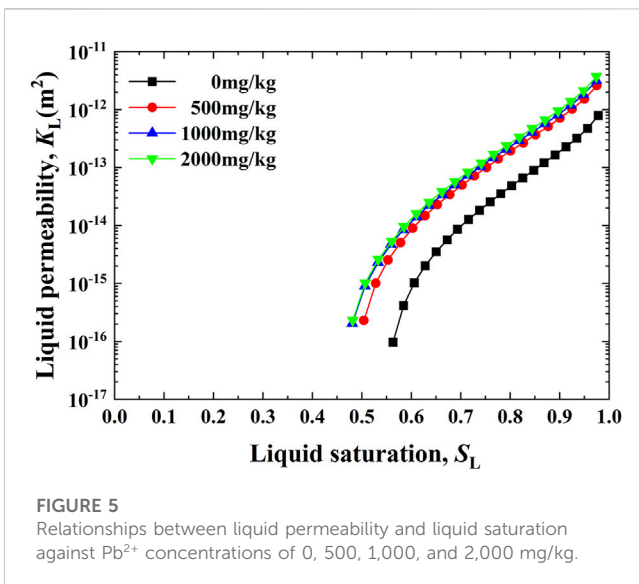
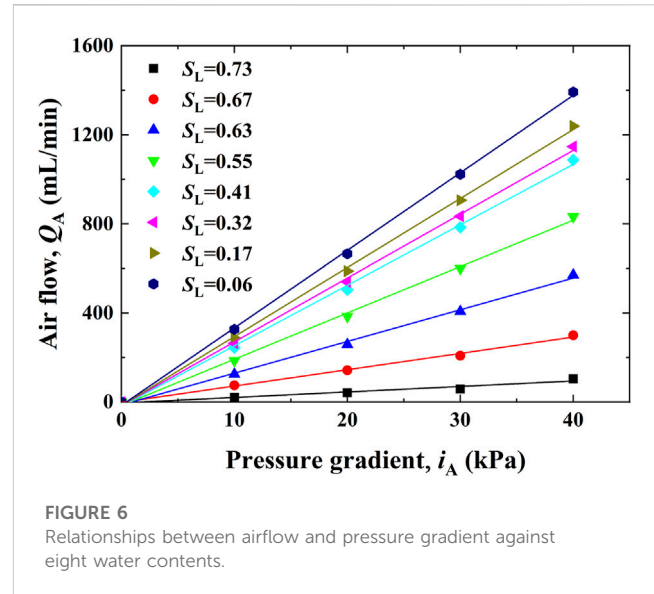
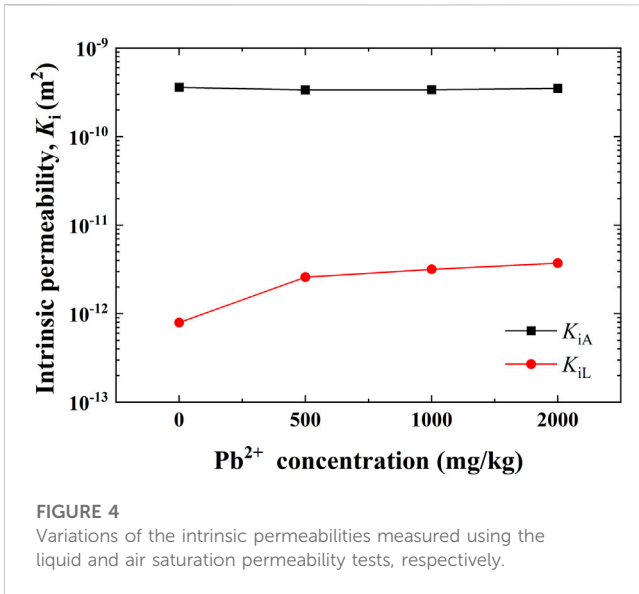
The soil–water characteristic curves for the Pb-contaminated loess against concentrations of 0, 500, 1,000, and 2,000 mg/kg, respectively, are shown in Figure 3A. The liquid saturation  $S_L$  shows a small change under lower suction  $s$  ranges (1–10 kPa), and under higher suction  $s$  ranges (10–1,000 kPa), it goes into a sharp decline. Furthermore, the decline under higher suction  $s$  ranges becomes more significant when  $Pb^{2+}$  concentration is increased.

The soil–water characteristic curves were fitted using the VG model. The best-fitting results are shown in Figures 3B–E. Given that the air entry value describes how difficult air can permeate into soil and squeeze pore water out, it is also indicated in each of the soil–water characteristic curves. The air entry value was derived

using the horizontal intercept of the extension of the high-suction asymptote. Generally, the soil–water characteristic curves are well-fitted with the VG model. Furthermore, the air entry value decreased from 22.2 to 11.6 kPa when the  $Pb^{2+}$  concentration changed from 0 to 2,000 mg/kg. The higher the  $Pb^{2+}$  concentration, the lower the air entry value, indicating that  $Pb^{2+}$  degrades the water retention behavior of the loess, and the degradation in the water retention behavior becomes more significant when subjected to higher  $Pb^{2+}$  concentrations.

### 3.2 Liquid and air permeability

Figure 4 shows the variations in the intrinsic permeabilities  $K_{iA}$  and  $K_{iL}$  against  $Pb^{2+}$  concentrations of 0, 500, 1,000, and 2,000 mg/kg, measured by the liquid and air saturation permeability tests, respectively. The experimental results indicated



that  $K_{iL}$  increased from  $3.73 \times 10^{-12} \text{ m}^2$  to  $7.92 \times 10^{-13} \text{ m}^2$  with the increase in the  $Pb^{2+}$  concentration, and the magnitude could be as high as approximately one order. Furthermore,  $K_{iA}$  shows a small change, indicating that  $Pb^{2+}$  concentration has a minimal effect on  $K_{iA}$ .

The relationships between the liquid permeability  $K_L$  and the liquid saturation  $S_L$  for the Pb-contaminated loess are shown in Figure 5.  $K_L$  increases with the increase in  $S_L$ , with a rate higher for a 0.45–0.65 range and a rate lower for a 0.65–1.0 range. Furthermore, for a given  $S_L$ , the higher the concentration of  $Pb^{2+}$ , the higher the value of  $K_L$ . Conversely, the relationships between the air flow  $Q_A$  and the pressure gradient  $i_A$  against  $S_L$  ranging from 0.06 to 0.73 are shown in Figure 6. It is evident that  $Q_A$  behaves in a linear relationship with  $i_A$ . In other words, airflows in our permeability tests can still be described by Darcy's law. As a result, the

relationships between  $K_A$  determined using Darcy's law (Eq. 8 and Eq. 9) and  $S_L$  for the Pb-contaminated loess are shown in Figure 7.  $K_A$  generally decreases with an increase in  $S_L$ . Its rate is moderate for a 0.1–0.6 range and becomes more significant for a 0.6–0.8 range. It is also observed that the rate differs significantly from each other, most likely due to the change in microstructure (see the enlargement shown in Figure 7). Furthermore, for a given  $S_L$ , the higher the concentration of  $Pb^{2+}$ , the higher the value of  $K_A$ . It is worth noting that  $S_L$  corresponding to the curve turning point increases from 0.61 to 0.68 when  $Pb^{2+}$  concentration increases from 0 to 2,000 mg/kg, showing that  $Pb^{2+}$  concentration has some implications on  $K_A$ . This may be attributed to the connectivity of pore fluid channels.

### 3.3 Microscopic tests

The SEM images taken from the present work at a magnification of 500 times were binarised using Image-Pro Plus 6.0 software to extract microstructural parameters. The SEM images on the left represent the raw images, and those in the middle refer to the binarised images (Figures 8A–D). Those on the right show the distribution of the four pore categories. The distribution of the four pore categories is further analyzed in a quantitative manner, as shown in Figure 8E. The proportion of micropores decreases with the increase in  $Pb^{2+}$  concentration. In contrast, the proportion of mesopores increases with the increase in  $Pb^{2+}$  concentration.

The incremental pore volume curves derived from the MIP tests for the Pb-contaminated loess are rather similar to each other (Figure 9B). The difference in the cumulative pore volume curves is more significant for smaller pore size ranges than larger pore size ranges (Figure 9A). The proportion of the four pore categories against  $Pb^{2+}$  concentrations at 0, 500, 1,000, and 2,000 mg/kg, respectively, is shown in Figure 9C. The results of the MIP tests are almost in line with those derived from the analyzed results of the SEM images; the proportion of the micropores reduces with the

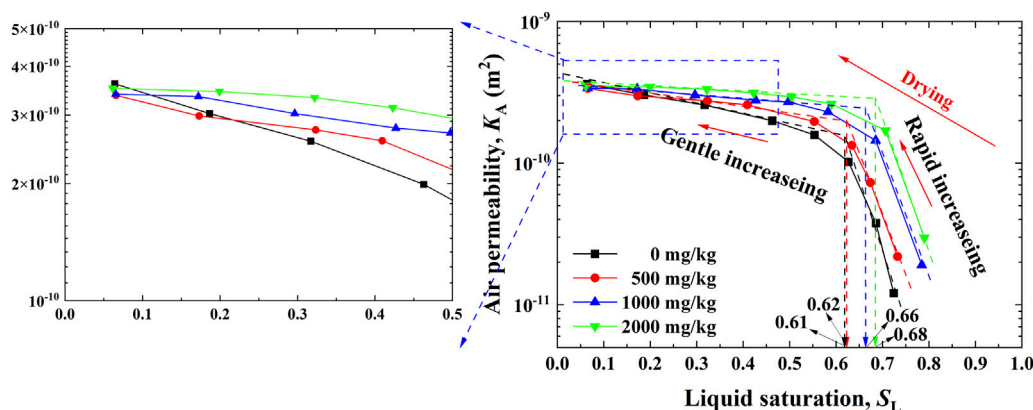


FIGURE 7

Relationships between air permeability and liquid saturation against  $Pb^{2+}$  concentrations of 0, 500, 1,000, and 2,000 mg/kg.

increasing  $Pb^{2+}$  concentration, whereas the proportion of the mesopores elevates with the increase in  $Pb^{2+}$  concentration.

The XRD test results for the uncontaminated and Pb-contaminated loess are shown in Figure 10. Six main minerals are identified: quartz, calcite, albite, illite, orthoclase, and kaolinite. Illite and kaolinite are identified at 10.0880 Å and 7.1439 Å, respectively, whereas calcite and orthoclase are recognized at 3.0437 Å and 3.7923 Å, respectively. Furthermore, the intensity against illite, kaolinite, albite, orthoclase, and calcite reduces with the increase in  $Pb^{2+}$  concentration, and the diffractogram of the Pb-contaminated loess shows two new reflections at  $2\theta = 25.419^\circ$  and  $2\theta = 30.776^\circ$ , respectively, corresponding to the formation of cerussite. Wang et al. (2016) observed a similar phenomenon. Moreover, the inter-layer spacing against the minerals increases with the increasing  $Pb^{2+}$  concentration, as indicated by the analyzed results based on MDI Jade software. Li et al. (2015) also identified the increase in inter-layer spacing.

The results of the SEM-EDS tests for the uncontaminated loess and contaminated loess are shown in Figure 11. The content of sodium, calcium, magnesium, aluminum, and potassium ions generally decreases with the increase in  $Pb^{2+}$  concentration. To interpret this part in more detail the content change in chemical components and the cation concentration in pore fluid, the leachate, derived right after the permeability tests, was analyzed in terms of cation concentration. The results show that  $Na^+$  and  $Ca^{2+}$  concentrations increase with the increase in  $Pb^{2+}$  concentration, whereas  $K^+$  and  $Mg^{2+}$  concentrations show a small change (Figure 12).

The zeta potential for the Pb-contaminated loess against concentrations of 0, 500, 1,000, and 2,000 mg/kg is presented in Figure 13. The absolute  $\zeta$  value decreases with increasing  $Pb^{2+}$  concentration. Given the  $Pb^{2+}$  concentration of 500 mg/kg, the absolute  $\zeta$  value decreases rapidly, from 15.7 mV of the natural loess to 11.9 mV. When the  $Pb^{2+}$  concentration increases to 1,000 mg/kg, the absolute  $\zeta$  value decreases from 11.9 to 11.4 mV, and the rate of decrease becomes slow. When the lead concentration is greater than 1,000 mg/kg, the absolute  $\zeta$  value stabilizes at approximately 11.2 mV.

## 4 Discussion

### 4.1 Water retention behavior

The intrinsic permeability is dependent mainly upon pore size, pore geometry, and pore size distribution (Lu & Likos, 2004). In the present work,  $K_{iA}$  is much higher than  $K_{iL}$ , and their difference can be as high as two orders of magnitude, which is in line with observations carried out by Stoltz et al. (2010), Xu et al. (2014), and Zhang D. F. et al. (2020) (Figure 4). The formation of their differences is most likely because of air slippage and pore fluid polarity (Xu et al., 2014). Air slippage can reduce the friction of airflow and, therefore, accelerates its flow rate. In some cases, air slippage can aggravate measurement error to greater than 10% as the intrinsic permeability is less than  $10^{-13} \text{ m}^2$  (Klinkenberg, 1941; Fredlund et al., 2012). This leads to a non-Darcy flow phenomenon when measuring permeability with air. However, in our experiments, the measured air permeability conforms to Darcy's law (Figure 6). Correction for air slippage is deemed unnecessary for high-permeability soils (Fredlund et al., 2012). Therefore, in the present work, the effect of air slippage can be neglected because the intrinsic permeability  $K_{iA}$  is measured as approximately  $3.4 \times 10^{-10} \text{ m}^2$ , which is three orders of magnitude larger than  $10^{-13} \text{ m}^2$ . Conversely, the asymmetric distribution of the two hydrogen and oxygen atoms results in water being a polar molecule that can form hydrogen bonds with adjacent molecules, leading to the presence of surface tension and capillary forces. Wojnarowski et al. (2018) found that water adsorption on the surface of porous media leads to a decrease in its effective channel radius, which causes some smaller pore channels, allowing airflows but not water flows. As indicated by our experiments, the intrinsic permeability measured using water is smaller than that measured using air. Clay soil features a negatively charged surface, and pore fluid with polarity may interact with the negatively charged surface. For example, pore water, categorized as one of the "polar" fluids, may be absorbed by hydrogen bonds formed on the clay surface. To this end, the majority of flow channels become narrower or even clogged to cause an increase in the friction of liquid flow and then reduce the intrinsic permeability. However, air (corresponding to one of the "non-polar" fluids) has a rather small tendency to be adsorbed by clay soil, causing the majority of flow channels to become wider and

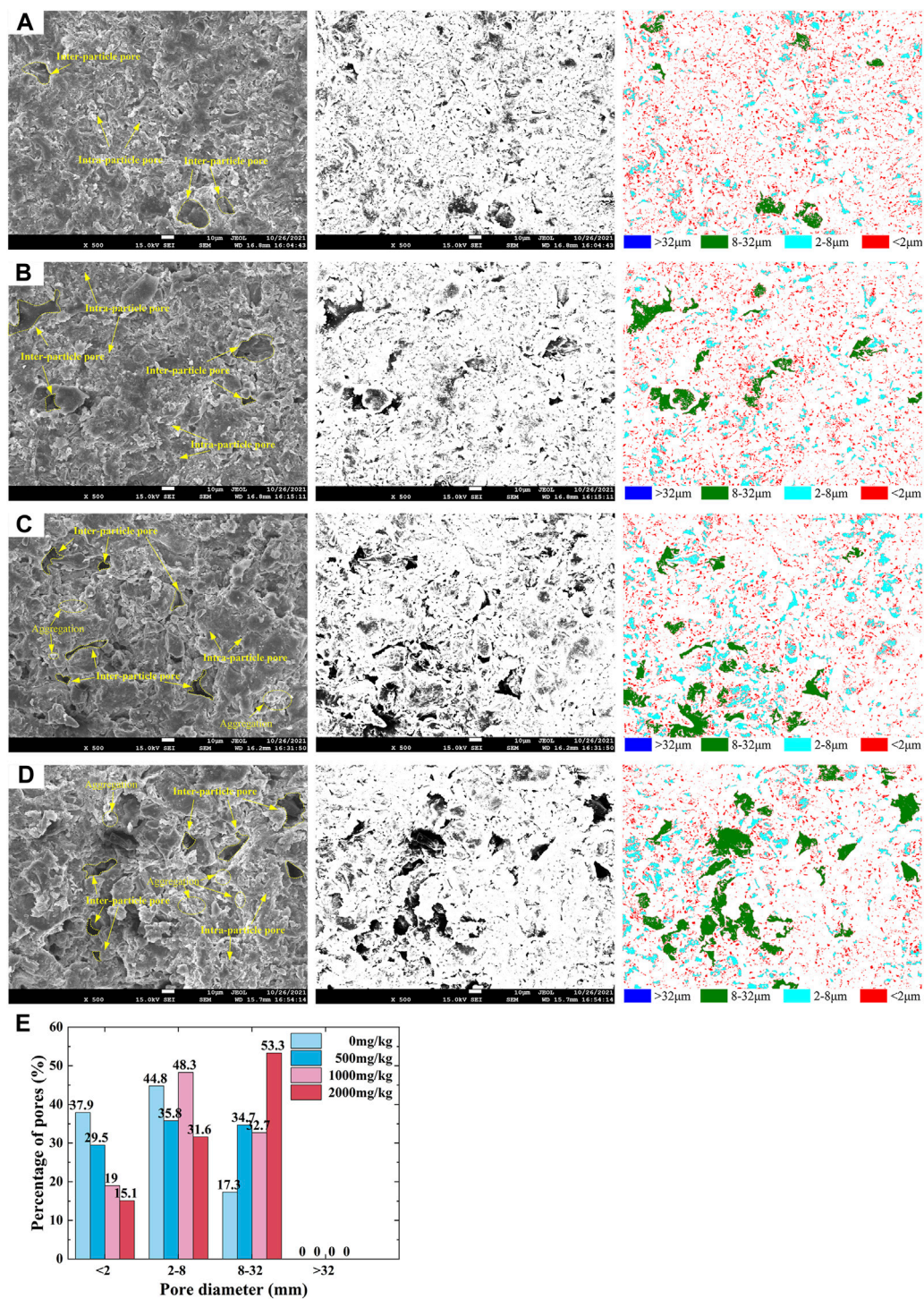
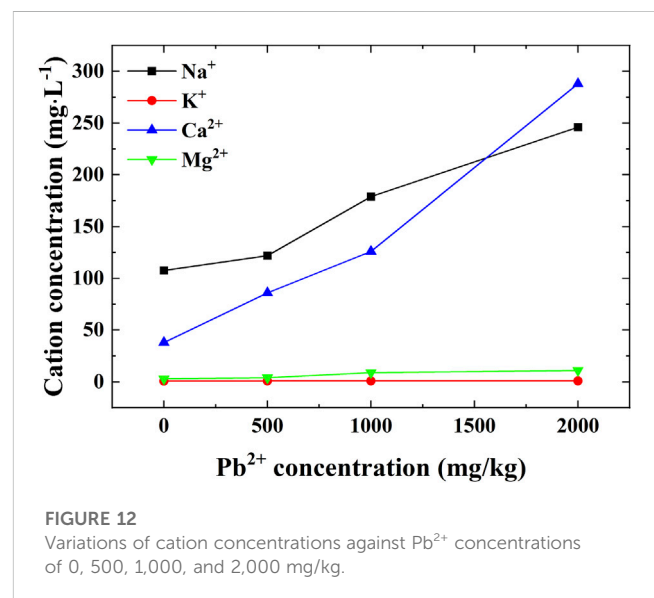
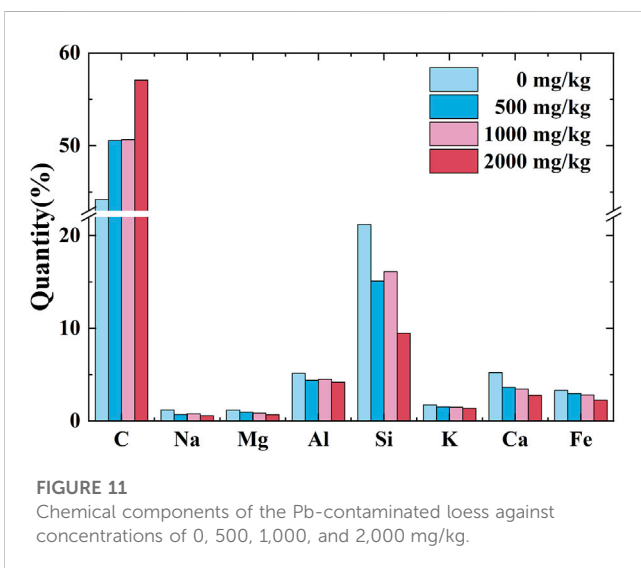
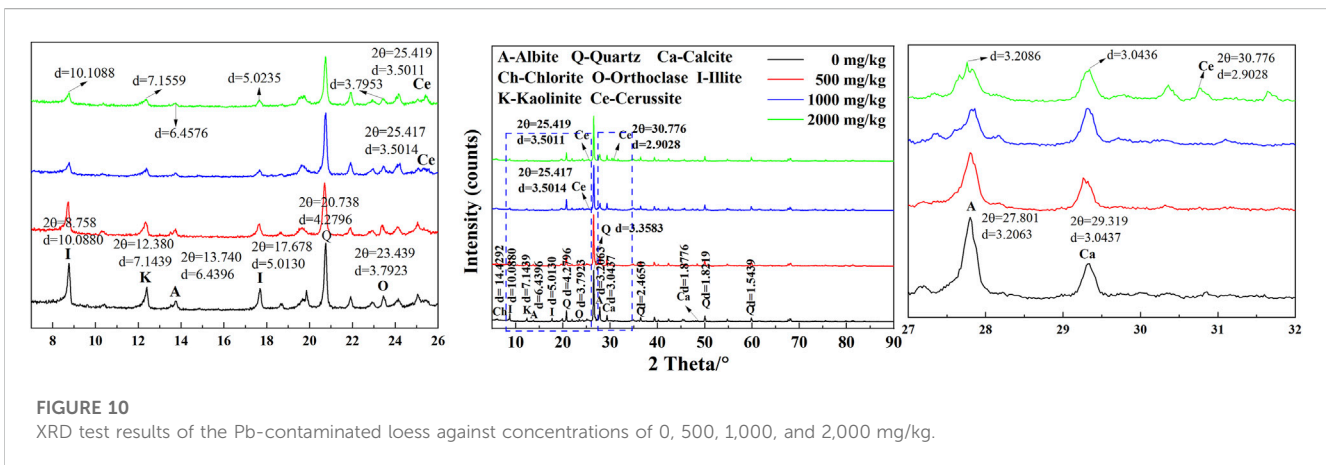
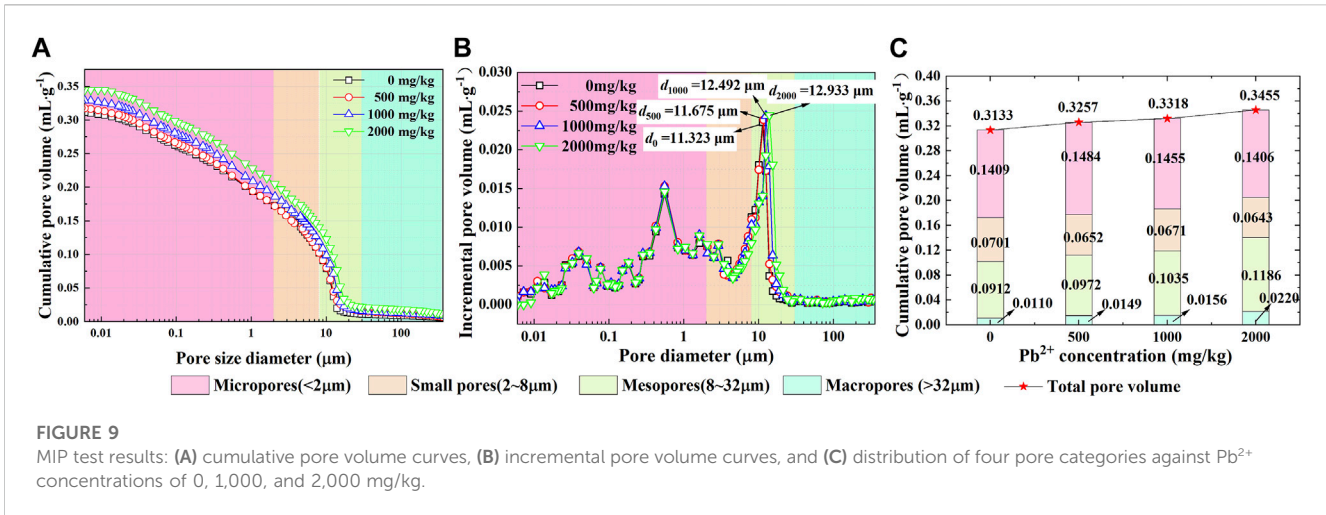


**FIGURE 8** Scanning electron microscopic images: (A) loess contaminated by Pb<sup>2+</sup> of 0 mg/kg; (B) loess contaminated by Pb<sup>2+</sup> of 500 mg/kg; (C) loess contaminated by Pb<sup>2+</sup> of 1,000 mg/kg; (D) loess contaminated by Pb<sup>2+</sup> of 2,000 mg/kg; and (E) distributions of micropore, small pore, mesopores, and macropore for the Pb-contaminated loess.

increasing the intrinsic permeability. As a result, for porous media, the intrinsic permeability determined primarily relies not only on the pore structure but also on polarity.

The DDL theory is deemed useful in interpreting microscale structural evolution when subjected to the effect of seepage

conditions and establishing its linkage to the macroscale permeability properties (Li et al., 2015). Water molecules (polar fluid) and cations are adsorbed onto the surface of negatively charged clay particles and arranged in a directional manner, as depicted in Figure 14A. It is widely acknowledged that the



electrostatic attraction is the strongest near the surface of particles, and the hydrated cations due to the electrostatic attraction force are firmly adsorbed onto the surface of particles to form the Stern layer. The greater the distance from particles, the smaller the attraction

force. To this end, for those farther from the particle, their activity is not as restricted as that in the Stern layer, thereby defining the Gouy layer. As indicated by the present literature (Brian and Ernest, 2004; Liu et al., 2017; Darrow et al., 2020), the slippage of water molecules

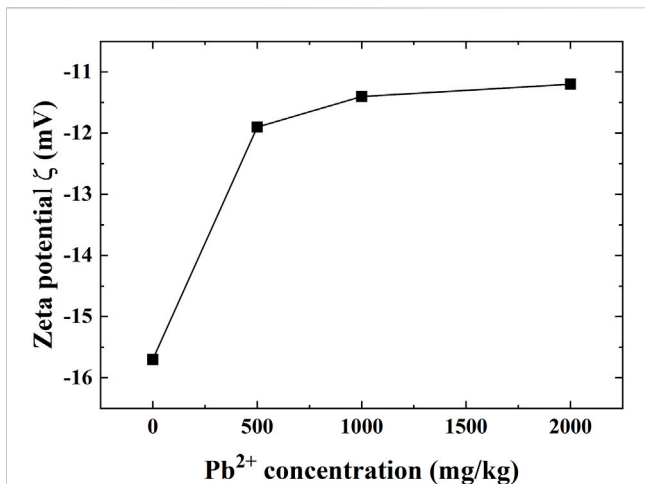


**FIGURE 13**  
Zeta test results of the Pb-contaminated loess against concentrations of 0, 500, 1,000, 2,000 mg/kg.

pH value, valence state, ion properties, and ion concentration. The concentration and valence of cations in the pore fluid of loess increase when contaminated by Pb<sup>2+</sup> (Figure 12). Under the action of potential energy and electrostatic attraction, Pb<sup>2+</sup> intrudes into the DDL with cation exchange, which results in the disintegration and transformation of minerals (Figure 10). In other words, the intrusion of Pb<sup>2+</sup> increases the concentration and valence of cations in the DDL, which can neutralize more electric charges in the Stern layer, reduce the absolute zeta potential ζ, and make the DDL thinner (Figures 13, 14A). As a result, the van der Waals attraction between particles is greater than the repulsion force, leading to the agglomeration of clay particles and the widening of the pore channels (Figure 14B). In other words, the higher the concentration of Pb<sup>2+</sup>, the thinner the Gouy layer, and the more significant the agglomerated structure, which also indicates an increase in the intrinsic permeability and a decrease in the water retention ability. Conversely, due to the thinner Gouy layer, the minimum capillary diameter ( $D_{min}$ ) between two free interfaces for which the electrostatic attraction reaches a minimum is increased accordingly. Therefore, some new pore channels are developed. Macroscopically, it corresponds to an enhancement of the permeability of Pb-contaminated soil, a decrease in the air entry threshold, and a decrease in the water retention ability. On the whole, the water retention ability is found to behave in a descending manner. The effect of agglomerated structure formation goes against the water retention ability, whereas the effect of pore fluid polarity promotes it.

is easily present at a distance a bit farther from the Helmholtz plane that distinguishes the Gouy layer from the Stern layer, and this is referred to as the slipping plane. Considering the DDL features, a change in its thickness can occur when subjected to the effect of mineral and external conditions, including surface charge density,

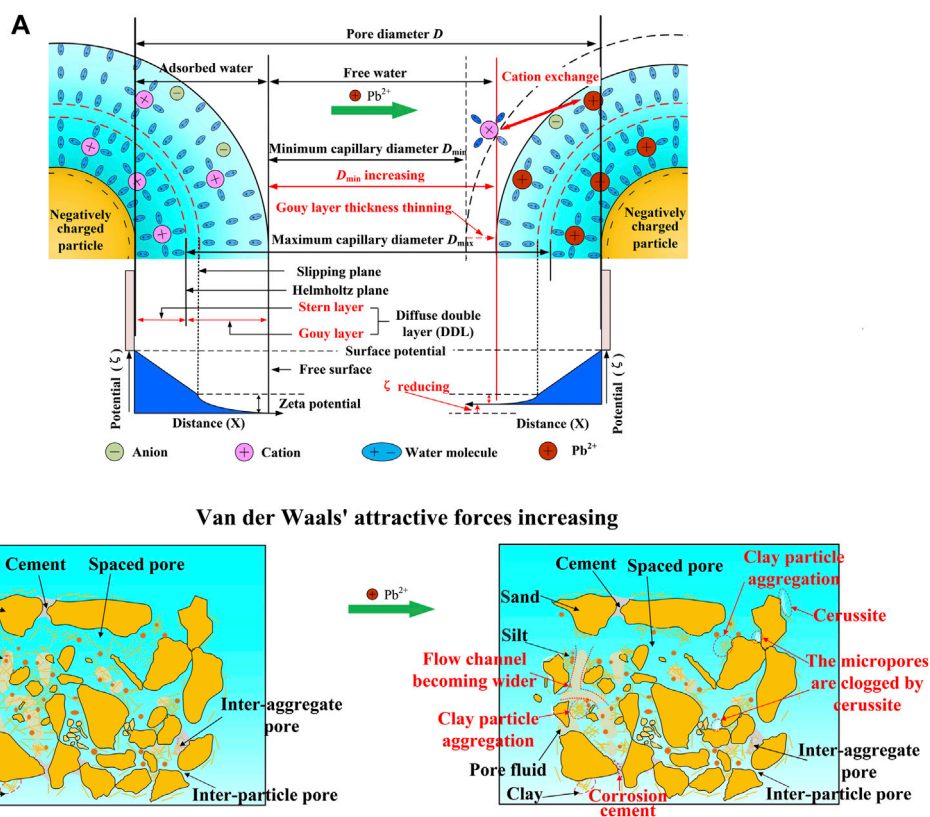


**FIGURE 14**  
Schematic illustration of microstructure changes when subjected to the effect of lead contamination: (A) diffuse double layer and (B) microstructure changes of loess.

## 4.2 Liquid and air permeability

Upon the saturated state, the saturated permeability associated with free pore water flowing only along the free surface to overcome the viscous force of the fluid itself is considered to be the maximum. As the air pressure increases but remains less than the air entry value, the change in contact angle results in an increase in matrix suction. At this time, the fluid overcomes its own viscous force, although it is influenced by the matrix suction. When subjected to air pressure higher than the air entry value, the liquid overflows, and therefore, the soil enters an unsaturated state where the capillary action occurs. Considering water molecules farther than the free interface, their movement regime is not governed by the electrostatic attraction but by the Brownian motion. Therefore, they can be regarded as free pore water. Due to the capillary action, the free interface moves inwards. The liquid flow needs to overcome its own viscous force and the matrix suction to mitigate the effect of adsorption. The permeability of loess decreases rapidly as water in macropores and mesopores overflows in the first place. The permeability reduces further to a minimum when the water occupying micropores overflows afterward, although the adsorption of particles may impede such water overflowing. These arguments aim to describe how the permeability changes when transferred from a saturated state to an unsaturated state, and a detailed discussion on  $K_L$  and  $K_A$  is given as follows.

$K_L$  behaving in an ascending tendency is just opposite to  $K_A$  behaving in a descending tendency when  $S_L$  is increased, most likely due to pore fluid connectivity (Figures 5, 7). When under a high liquid saturation (i.e.,  $S_L > 0.8$ ), the pore water is sufficient and distributed uniformly, thereby increasing the polar fluid connectivity and subsequently degrading the non-polar fluid connectivity. The non-polar fluid becomes continuous when  $S_L$  is reduced to about 85% toward initiating the airflow (Fredlund and Rahardjo, 1993). As  $S_L$  ranges between 0.6 and 0.8, air and water flows are present at the same time, indicating that the air and water flows reach a quasi-equilibrium condition (Zhan et al., 2014; Chen et al., 2017; Zhang D. F. et al., 2020). When under a low liquid saturation (i.e.,  $S_L < 0.6$ ), the pore water is not sufficient and distributed in a scattered manner, hence causing some difficulty in increasing the polar fluid connectivity and subsequently increasing the non-polar fluid connectivity. These results satisfactorily address the change in  $K_L$  and  $K_A$ .

Given that the dolomite-rich loess is widely distributed across Northwest China (Wang et al., 2022),  $\text{Ca}(\text{HCO}_3)_2$  and  $\text{Mg}(\text{HCO}_3)_2$  are discharged when the leaching of dolomite is initiated by the permeability tests (Eq. 10). Their dissolution discharges  $\text{Ca}^{2+}$  and  $\text{Mg}^{2+}$  (Eqs 11 and 12), and they could, however, react with dolomite again to discharge  $\text{Mg}^{2+}$  and precipitate  $\text{CaCO}_3$  (referred to as “dedolomitization”) (Eq. 13). In other words, dedolomitization is a physicochemical process of transforming dolomite to calcite through the effect of Ca-rich or Mg-rich water leaching. When subjected to the effect of  $\text{Pb}^{2+}$ , the ion exchange between sodium, calcium magnesium, aluminum, and lead ions causes morphology and structural changes in minerals included in the loess.  $\text{CaCO}_3$  transforms to  $\text{PbCO}_3$  due to its higher solubility product (Figure 10 and Eq. 14). Therefore, micropores are clogged by  $\text{PbCO}_3$ , leading to the reduction in the proportion of micropores (Figures 8E, 9C). In addition,  $\text{PbCO}_3$  is deposited on the surface of the soil particles,



forming a slow-release layer (Figure 14B). These results satisfactorily explain the changes in the enlargement shown in Figure 7 and the absolute  $\zeta$  value shown in Figure 13. On the other hand, the intrinsic characteristics of clay minerals enhance the adsorption properties of lead ions along the external hydroxyl surface, and a part of  $\text{H}^+$  ions are discharged (Frost, 1998) (Eqs 15 and 16).  $\text{H}^+$  ions discharge causes damage to the cementation between particles due to their corrosion, resulting in an increase in the fraction of mesopores and a deterioration of the microstructural characteristics.

## 4.3 Summary

The effect of pore fluid polarity causes the majority of flow channels to become narrower or even clogged, reducing the intrinsic permeability determined by the liquid. In addition,  $\text{Pb}^{2+}$  can neutralize more electric charges and, therefore, reduce the absolute zeta potential  $\zeta$  (Figure 13). As a result, the Gouy layer becomes thinner than before, which promotes the formation of an agglomerated structure. The more significant the agglomerated structure, the higher the intrinsic permeability. The results of the SEM and MIP tests are in good agreement with those derived from the permeability tests; the proportion of the micropores reduces as a consequence of the precipitation of  $\text{PbCO}_3$ , resulting from the dedolomitization and cation exchange, whereas the proportion of the mesopores elevates with the increasing  $\text{Pb}^{2+}$  concentration because of the corrosion of  $\text{H}^+$ . The change in the liquid and air permeability properties shows a strong correspondence to the microscale structural evolution when subjected to the effect of lead contamination.

## 5 Conclusion

This work investigated the effect of lead contamination on the microstructure and air and liquid permeability of the loess. The microscale structural evolution corresponded well to the macroscale air and liquid permeability properties. Based on the results and discussion, some main conclusions can be drawn as follows:

- (1) The effect of pore fluid polarity plays a leading role in modifying the air and liquid permeability properties of Pb-contaminated loess. The airflow has a rather small tendency to be adsorbed by clay soil, making the majority of flow channels wider and increasing the intrinsic permeability. In contrast, the pore fluid narrows flow channels or raises their clogging potential.

The intrinsic permeability measured in airflows is higher than that measured in liquid flows. Furthermore, the agglomerated structure formation, induced by the reduction in the absolute zeta potential  $\zeta$  resulting from the intrusion of  $\text{Pb}^{2+}$ , also increases the intrinsic permeability.

- (2) The results of microscopic tests show that the physicochemical reactions between  $\text{Pb}^{2+}$  and loess lead to mineral disintegration and transformation, causing cerussite precipitation ( $\text{PbCO}_3$ ). The pore structure of the Pb-contaminated soil, due to the corrosion induced by  $\text{H}^+$ , evolves from small pores to mesopores, and the total pore volume increases, reducing air entry value and degrading water retention behavior.
- (3) The higher the liquid saturation ( $S_L > 0.8$ ), the higher the polar fluid connectivity, and the lower the non-polar fluid connectivity. The air and water flows reach a quasi-equilibrium condition when  $S_L$  falls within the 0.6–0.8 range. Under a low liquid saturation ( $S_L < 0.6$ ), the pore water is distributed in a scattered manner, thereby increasing the non-polar fluid connectivity.
- (4) The dedolomitization of transforming dolomite to calcite through the effect of Ca-rich or Mg-rich water leaching notably affects the distribution of pores, and  $\text{PbCO}_3$  precipitation induced by the dedolomitization clogs the micropores. A part of  $\text{H}^+$  ions is discharged, and they cause damage to the cementation between particles, increasing the fraction of mesopores. The change in the liquid and air permeability properties presents a strong correspondence to the microscale structural evolution. Such a microscale structural evolution may change when subjected to other metals.

## Data availability statement

The original contributions presented in the study are included in the article/[Supplementary Material](#). further inquiries can be directed to the corresponding author.

## Author contributions

SW: data curation, formal analysis, validation, software, and writing—original draft. W-CC: conceptualization, methodology,

writing—review and editing, supervision, and funding acquisition. WH: data curation, formal analysis, validation, software, and writing—original draft. MR: writing—review and editing and supervision. All authors contributed to the article and approved the submitted version.

## Funding

This research was supported by the Shaanxi Educational Department (2020TD-005) and the Shaanxi Housing and Urban-Rural Development Office (2018-K15).

## Acknowledgments

This study is based on work supported by the Shaanxi Educational Department (2020TD-005) and the Shaanxi Housing and Urban-Rural Development Office (2018-K15).

## Conflict of interest

The authors declare that the research was conducted in the absence of any commercial or financial relationships that could be construed as a potential conflict of interest.

## Publisher's note

All claims expressed in this article are solely those of the authors and do not necessarily represent those of their affiliated organizations or those of the publisher, the editors, and the reviewers. Any product that may be evaluated in this article, or claim that may be made by its manufacturer, is not guaranteed or endorsed by the publisher.

## Supplementary material

The Supplementary Material for this article can be found online at: <https://www.frontiersin.org/articles/10.3389/feart.2023.1165685/full#supplementary-material>

## References

- ASTM (2021). *Standard test method for particle-size distribution (gradation) of fine-grained soils using the sedimentation (hydrometer) analysis*. West Conshohocken, Pa: American Society for Testing and Materials. ASTM standard D7928-21e1. doi:10.1520/D7928-21E01
- ASTM (2010). *Standard test methods for particle-size distribution (gradation) of soils using sieve analysis*. West Conshohocken, Pa: American Society for Testing and Materials. ASTM standard D6913-04e1. doi:10.1520/D6913-04E01
- Bai, B., Bai, F., Li, X., Nie, Q., and Jia, X. (2022). The remediation efficiency of heavy metal pollutants in water by industrial red mud particle waste. *Environ. Technol. Innov.* 28, 102944. doi:10.1016/j.eti.2022.102944
- Bai, X. D., Cheng, W. C., and Li, G. (2021). A comparative study of different machine learning algorithms in predicting EPB shield behaviour: a case study at the Xi'an metro, China. *Acta Geotech.* 16 (12), 4061–4080. doi:10.1007/s11440-021-01383-7
- Bian, R. X., Chen, J. H., Li, W. H., Sun, Y. J., Chai, X. L., Wang, H. W., et al. (2021). Numerical modeling of methane oxidation and emission from landfill cover soil coupling water-heat-gas transfer: Effects of meteorological factors. *Process Saf. Environ. Prot.* 146, 647–655. doi:10.1016/j.psep.2020.11.052
- Brian, J. K., and Ernest, F. H. (2004). Zeta potential of microfluidic substrates: 1. Theory, experimental techniques, and effects on separations. *Electrophoresis* 25 (2), 187–202. doi:10.1002/elps.200305754
- Burakov, A. E., Galunin, E. V., Burakova, I. V., Kucherova, A. E., Gupta, V. K., Tkachev, A. G., et al. (2017). Adsorption of heavy metals on conventional and nanostructured materials for wastewater treatment purposes: A review. *Ecotoxicol. Environ. Saf.* 148, 702–712. doi:10.1016/j.ecoenv.2017.11.034
- Cai, G. Q., Zhou, A. N., and Sheng, D. C. (2014). Permeability function for unsaturated soils with different initial densities. *Can. Geotechnical J.* 51 (12), 1456–1467. doi:10.1139/cgj-2013-0410
- Chen, C. L., Zhang, D. F., and Zhang, J. (2017). Influence of stress and water content on air permeability of intact loess. *Can. Geotechnical J.* 54 (9), 1221–1230. doi:10.1139/cgj-2016-0186
- Chen, Y. Z., Zhou, W. H., Liu, F. M., Yi, S. P., and Geng, X. Y. (2019). Microstructure and morphological characterization of lead-contaminated clay with nanoscale zero-valent iron (nZVI) treatment. *Eng. Geol.* 256, 84–92. doi:10.1016/j.enggeo.2019.05.001

- Darrow, M. M., Guo, R., and Trainor, T. P. (2020). Zeta potential of cation-treated soils and its implication on unfrozen water mobility. *Cold Regions Sci. Technol.* 173, 103029. doi:10.1016/j.coldregions.2020.103029
- Du, Y. J., Wei, M. L., Reddy, K. R., Reddy, K. R., and Wu, H. L. (2016). Effect of carbonation on leachability, strength and microstructural characteristics of KMP binder stabilized Zn and Pb contaminated soils. *Chemosphere* 144, 1033–1042. doi:10.1016/j.chemosphere.2015.09.082
- Dutta, J., and Mishra, A. K. (2016). Influence of the presence of heavy metals on the behaviour of bentonites. *Environ. Earth Sci.* 75 (11), 993–1010. doi:10.1007/s12665-016-5811-2
- Elhakim, A. F. (2016). Estimation of soil permeability. *Alexandria Eng. J.* 55 (3), 2631–2638. doi:10.1016/j.aej.2016.07.034
- Fredlund, D. G., Rahardjo, H., and Fredlund, M. D. (2012). *Unsaturated soil mechanics in engineering practice*. Canada: John Wiley & Sons.
- Fredlund, D. G., and Rahardjo, H. (1993). *Soil mechanics for unsaturated soils*. New York: Wiley Publication.
- Fredlund, D. G., Xing, A. Q., and Huang, S. Y. (1994). Predicting the permeability function for unsaturated soils using the soil-water characteristic curve. *Can. Geotechnical J.* 31 (4), 533–546. doi:10.1139/t94-062
- Frost, R. L. (1998). Hydroxyl deformation in kaolins. *Clays Clay Min.* 46 (3), 280–289. doi:10.1346/CCMN.1998.0460307
- Gao, J. L., Oloibiri, V., Chys, M., Audenaert, W., Decostere, B., He, Y. L., et al. (2015). The present status of landfill leachate treatment and its development trend from a technological point of view. *Rev. Environ. Sci. Biotechnol.* 14 (1), 93–122. doi:10.1007/s11157-014-9349-z
- Gao, Y. Y., Qian, H., Li, X. Y., Chen, J., and Jia, H. (2018). Effects of lime treatment on the hydraulic conductivity and microstructure of loess. *Environ. Earth Sci.* 77, 529. doi:10.1007/s12665-018-7715-9
- Hong, B., Li, X. A., Wang, L., and Li, L. C. (2019). Temporal variation in the permeability anisotropy behavior of the malan loess in northern Shaanxi province, China: An experimental study. *Environ. Earth Sci.* 78, 447. doi:10.1007/s12665-019-8449-z
- Hu, W., Cheng, W. C., and Wen, S. (2022). Investigating the effect of degree of compaction, initial water content, and electric field intensity on electrokinetic remediation of an artificially Cu- and Pb-contaminated loess. *Acta Geotechnica*. doi:10.1007/s11440-022-01602-9
- Hu, W., Cheng, W. C., Wang, Y., and Wen, S. (2023). Feasibility study of applying a graphene oxide-alginate composite hydrogel to electrokinetic remediation of Cu(II)-contaminated loess as electrodes. *Sep. Purif. Technol.* 322, 124361. doi:10.1016/j.seppur.2023.124361
- Klinkenberg, L. J. (1941). *The permeability of porous media to liquids and gases*. New York: American Petroleum Institute.
- Laner, D., Crest, M., Scharff, H., Morris, J. W. F., and Barlaz, M. A. (2012). A review of approaches for the long-term management of municipal solid waste landfills. *Waste Manag.* 32, 498–512. doi:10.1016/j.wasman.2011.11.010
- Lei, X. Y. (1987). The types of loess pores in China and their relationship with collapsibility. *Sci. China B* 17 (12), 1309–1318. (in Chinese).
- Li, J. S., Xue, Q., Wang, P., and Li, Z. Z. (2015). Effect of lead (II) on the mechanical behavior and microstructure development of a Chinese clay. *Appl. Clay Sci.* 105–106, 192–199. doi:10.1016/j.clay.2014.12.030
- Liu, X. M., Ding, W. Q., Tian, R., Du, W., and Li, H. (2017). Position of shear plane at the clay–water interface: Strong polarization effects of counterions. *Soil Sci. Soc. Am. J.* 81 (2), 268–276. doi:10.2136/sssaj2016.08.0261
- Liu, Y. F., and Jeng, D. S. (2019). Pore scale study of the influence of particle geometry on soil permeability. *Adv. Water Resour.* 129 (7), 232–249. doi:10.1016/j.advwatres.2019.05.024
- Lu, N., and Likos, W. J. (2004). *Unsaturated soil mechanics*. Canada: John Wiley & Sons.
- Moon, S., Nam, K., Kim, J. Y., Hwan, S. K., and Chung, M. (2007). Effectiveness of compacted soil liner as a gas barrier layer in the landfill final cover system. *Waste Manag.* 28 (10), 1909–1914. doi:10.1016/j.wasman.2007.08.021
- Naveen, B. P., Mahapatra, D. M., Sitharam, T. G., Sivapullaiah, P. V., and Ramachandra, T. V. (2017). Physico-chemical and biological characterization of urban municipal landfill leachate. *Environ. Pollut.* 220, 1–12. doi:10.1016/j.envpol.2016.09.002
- NBS-PRC (National Bureau of Statistics of the People's Republic of China) (2021). *Population: Urban and rural population*. Resources & Environment: MSW collection and management. Available at: <http://www.stats.gov.cn/tjsj/ndsj/2021/indexch.htm>.
- Negi, P., Mor, S., Ravindra, K., and Hens, L. (2020). Impact of landfill leachate on the groundwater quality in three cities of North India and health risk assessment. *Environ. Dev. Sustain.* 22 (2), 1455–1474. doi:10.1007/s10668-018-0257-1
- Pandey, P., Lynch, K., Sivakumar, V., Solan, B., Nanda, S., et al. (2021). Measurements of permeability of saturated and unsaturated soils. *Géotechnique* 71 (2), 170–177. doi:10.1680/jgeot.19.P.058
- Pareja, C. J., Mateo, R., and Rodríguez, E. J. (2014). Lead (Pb) in sheep exposed to mining pollution: Implications for animal and human health. *Ecotoxicol. Environ. Saf.* 108, 210–216. doi:10.1016/j.ecoenv.2014.07.014
- Shi, L., Chen, H. X., Meng, H. L., Cheng, R., Dai, J. G., Zheng, X., et al. (2021). How environmental policy impacts technology adoption: A case of landfill leachate. *J. Clean. Prod.* 310, 127484. doi:10.1016/j.jclepro.2021.127484
- Souli, H., Fleureau, J. M., Ayadi, M. T., and Besnard, M. (2008). Physicochemical analysis of permeability changes in the presence of zinc. *Geoderma* 145 (1–2), 1–7. doi:10.1016/j.geoderma.2008.02.014
- Stoltz, G., Gourc, J. P., and Oxarango, L. (2010). Liquid and gas permeabilities of unsaturated municipal solid waste under compression. *J. Contam. Hydrology* 118 (1–2), 27–42. doi:10.1016/j.jconhyd.2010.07.008
- Tang, X. W., Zhen, Z. L., Chen, Y. M., and Wang, Y. (2008). Removal of Cu(II) from aqueous solution by adsorption on Chinese quaternary loess: Kinetics and equilibrium studies. *Environ. Lett.* 43 (7), 779–791. doi:10.1080/10934520801960144
- Taylor, M. P., Mackay, A. K., Hudson-Edwards, K. A., and Holz, E. (2010). Soil Cd, Cu, Pb and Zn contaminants around Mount Isa city, Queensland, Australia: Potential sources and risks to human health. *Appl. Geochem.* 25 (6), 841–855. doi:10.1016/j.apgeochem.2010.03.003
- Van Genuchten, M. T. (1980). A closed-form equation for predicting the hydraulic conductivity of unsaturated soils. *Soil Sci. Soc. Am. J.* 44 (5), 892–898. doi:10.2136/sssaj1980.03615995004400050002x
- Wang, H. K., Qian, H., and Gao, Y. (2020a). Non-darcian flow in loess at low hydraulic gradient. *Eng. Geol.* 267, 105483. doi:10.1016/j.enggeo.2020.105483
- Wang, J. D., Zhang, D. F., Chen, C. L., and Wang, S. (2020b). Measurement and modelling of stress-dependent water permeability of collapsible loess in China. *Eng. Geol.* 266, 105393. doi:10.1016/j.enggeo.2019.105393
- Wang, L., Cheng, W. C., Hu, W. L., Wen, S. J., and Shang, S. (2022). Effect of seepage conditions on the microstructural evolution of loess across north-west China. *IScience* 25, 104691. doi:10.1016/j.isci.2022.104691
- Wang, L., Cheng, W. C., Xue, Z. F., Xie, Y. X., and Lv, X. J. (2023). Feasibility study of applying electrokinetic technology coupled with enzyme-induced carbonate precipitation treatment to Cu- and Pb-contaminated loess remediation. *J. Clean. Prod.* 401, 136734. doi:10.1016/j.jclepro.2023.136734
- Wang, Y., Tang, X. W., Chen, Y. M., Zhan, L. T., Li, Z. Z., and Tang, Q. (2009). Adsorption behavior and mechanism of Cd (II) on loess soil from China. *J. Hazard. Mater.* 172 (1), 30–37. doi:10.1016/j.jhazmat.2009.06.121
- Wang, Y. Z., Chen, Y. M., Xie, H. J., Zhang, C. H., and Zhan, L. T. (2016). Lead adsorption and transport in loess-amended soil-bentonite cut-off wall. *Eng. Geol.* 215, 69–80. doi:10.1016/j.enggeo.2016.11.002
- Wei, Y. N., Fan, W., Yu, B., Deng, L. S., and Wei, T. (2020). Characterization and evolution of three-dimensional microstructure of Malan loess. *Catena* 192 (1), 104585. doi:10.1016/j.catena.2020.104585
- Wen, S. J., Cheng, W. C., Li, D. F., and Hu, W. L. (2023a). Immobilizing lead using loess and nanoscale zerovalent iron (nZVI)-amended loess: insights from macroscopic and microscopic tests. *Environ. Technol. Innov.* 31, 103228. doi:10.1016/j.eti.2023.103228
- Wen, S. J., Cheng, W. C., Li, D. F., and Hu, W. L. (2023b). Evaluating gas breakthrough pressure and gas permeability in a landfill cover layer for mitigation of hazardous gas emissions. *J. Environ. Manage.* 336, 117617. doi:10.1016/j.jenvman.2023.117617
- Wojnarowski, P., Czarnota, R., Janiga, D., and Stopa, J. (2018). Novel liquid-gas corrected permeability correlation for dolomite formation. *Int. J. Rock Mech. Min. Sci.* 112, 11–15. doi:10.1016/j.ijrmm.2018.10.004
- Xie, Y. X., Cheng, W. C., Wang, L., Xue, Z. F., Rahman, M. M., Hu, W., et al. (2023). Immobilizing copper in loess soil using microbial-induced carbonate precipitation: insights from test tube experiments and one-dimensional soil columns. *J. Hazard. Mater.* 444, 130417. doi:10.1016/j.jhazmat.2022.130417
- Xu, X. B., Zhan, T. L., Chen, Y. M., and Beaven, R. P. (2014). Intrinsic and relative permeabilities of shredded municipal solid wastes from the Qizishan landfill China. *Can. Geotechnical J.* 51 (11), 1243–1252. doi:10.1139/cgj-2013-0306
- Xu, L., Ye, W. M., Chen, Y. G., Chen, B., and Cui, Y. J. (2020a). Investigation on gas permeability of compacted GMZ bentonite with consideration of variations in liquid saturation, dry density and confining pressure. *J. Contam. Hydrology* 230, 103622. doi:10.1016/j.jconhyd.2020.103622
- Xu, J., Li, Y. F., Ren, C., and Lan, W. (2020b). Damage of saline intact loess after dry-wet and its interpretation based on SEM and NMR. *Soils Found.* 60 (4), 911–928. doi:10.1016/j.sandf.2020.06.006
- Xu, Y., Wu, Y. J., Zhang, X. D., and Chen, G. (2021a). Effects of freeze-thaw and chemical preconditioning on the consolidation properties and microstructure of landfill sludge. *Water Res.* 200 (3), 117249. doi:10.1016/j.watres.2021.117249
- Xu, P. P., Zhang, Q. Y., Qian, H., Li, M. N., and Yang, F. (2021b). An investigation into the relationship between saturated permeability and microstructure of remolded loess: A case study from Chinese Loess Plateau. *Geoderma* 382 (13), 114774. doi:10.1016/j.geoderma.2020.114774
- Xue, Z. F., Cheng, W. C., Xie, Y. X., Wang, L., Hu, W., and Zhang, B. (2023). Investigating immobilization efficiency of Pb in solution and loess soil using bio-inspired carbonate precipitation. *Environ. Pollut.* 322, 121218. doi:10.1016/j.envpol.2023.121218

- Xue, Z. F., Cheng, W. C., Wang, L., and Song, G. Y. (2021). Improvement of the shearing behaviour of loess using recycled straw fiber reinforcement. *KSCE J. Civ. Eng.* 25 (9), 3315–3339. doi:10.1007/s12205-021-2263-3
- Zha, F. S., Zhu, F. H., Xu, L., Kang, B., Yang, C. B., Zhang, W., et al. (2021). Laboratory study of strength, leaching, and electrical resistivity characteristics of heavy-metal contaminated soil. *Environ. Earth Sci.* 80 (5), 184–211. doi:10.1007/s12665-021-09451-7
- Zhan, L. T., Li, G. Y., Jiao, W. G., Tao, W., Lan, J. W., and Chen, Y. M. (2016). Field measurements of water storage capacity in a loess-gravel capillary barrier cover using rainfall simulation tests. *Can. Geotechnical J.* 54, 1523–1536. doi:10.1139/cgj-2016-0298
- Zhan, L. T., Qiu, Q. W., Yang, Y. B., Xu, W. J., and Chen, Y. M. (2017b). Soil column tests and numerical simulations of moisture-gas coupled flow in a loess cover. *J. Geotechnical Eng.* 39 (6), 969–977. doi:10.11779/CJGE201706001
- Zhan, L. T., Xu, H., Chen, Y. M., Lan, J. W., Lin, W. A., Xu, X. B., et al. (2017a). Biochemical, hydrological and mechanical behaviors of high food waste content MSW landfill: Preliminary findings from a large-scale experiment. *Waste Manag.* 68, 27–40. doi:10.1016/j.wasman.2017.03.008
- Zhan, L. T., Yang, Y. B., Chen, R., Ng, C. W. W., and Chen, Y. M. (2014). Influence of clod size and water content on gas permeability of a compacted loess. *Can. Geotechnical J.* 51 (12), 1468–1474. doi:10.1139/cgj-2014-0126
- Zhang, D. F., Wang, J. D., and Chen, C. L. (2020a). Gas and liquid permeability in the variably saturated compacted loess used as an earthen final cover material in landfills. *Waste Manag.* 105 (11), 49–60. doi:10.1016/j.wasman.2020.01.030
- Zhang, J., Zhang, S. H., and Xu, T. B. (2020b). Individual effect of matric suction on soil microstructure and hydraulic conductivity. *KSCE J. Civ. Eng.* 24, 1448–1459. doi:10.1007/s12205-020-1381-7
- Zhao, Y., Xue, Q., Huang, F. X., Hu, X. T., and Li, J. S. (2016). Experimental study on the microstructure and mechanical behaviors of leachate-polluted compacted clay. *Environ. Earth Sci.* 75 (12), 1006–1009. doi:10.1007/s12665-016-5816-x
- Zhou, C. Y., Yu, L., Huang, Z. R., Liu, Z., and Zhang, L. H. (2021). Analysis of microstructure and spatially dependent permeability of soft soil during consolidation deformation. *Soils Found.* 61 (3), 708–733. doi:10.1016/j.sandf.2021.02.004